38th ERF, September 4–7, 2012, Amsterdam, The Netherlands

052
Experimental-Numerical Investigation of the Dynamic Stall Phenomenon over the NACA 23012 Airfoil

A. Zanotti*, R. Nilifard, G. Gibertini, A. Guardone and G. Quaranta

Dipartimento di Ingegneria Aerospaziale – Politecnico di Milano
Via La Masa 34, 20156 Milano – Italy
e–mail: *zanotti@aero.polimi.it

Keywords: Dynamic stall, Computational fluid dynamics, Oscillating airfoils.

Abstract

The paper describes an experimental-numerical activity started at Politecnico di Milano about dynamic stall investigation. The main goal of this activity was to achieve a better insight in the phenomenon together with the evaluation of modeling capabilities comparing different two and three-dimensional numerical CFD models against experimental results. The experimental activity on a pitching NACA 23012 blade section model produced a comprehensive data set by means of two different techniques as unsteady pressure measurements and PIV. The numerical simulations were carried out with the EDGE code developed by FOI, the Swedish Defence Research Agency. The comparison of experimental and numerical results obtained for a pitching airfoil in deep dynamic stall conditions illustrates the capabilities of both a two and three-dimensional model to simulate this peculiar flow condition. In particular, the paper investigates the importance of three dimensional effects on the experiments.

Nomenclature

α	angle of attack [deg]
α_m	mean angle of attack [deg]
α_a	pitching oscillation amplitude [deg]
ω	circular frequency [rad/s]
b	blade section model span [m]
c	blade section model chord [m]
C_L	lift coefficient
C_M	pitching moment coefficient about the airfoil quarter chord
C_P	pressure coefficient
DSV	Dynamic Stall vortex
f	oscillation frequency [Hz]
k	reduced frequency $= \pi f c / U_\infty$
Ma	Mach number
N	number of grid points
PIV	Particle Image Velocimetry
Re	Reynolds number
U_∞	free-stream velocity [m/s]

1 Introduction

Several rotary-wing aircrafts design currently in advanced or preliminary development stage, such as the tiltrotor (Bell Boeing V-22, Bell Agusta BA609, ERICA concept) or the compound (Sikorsky X2, or the Eurocopter X3), call for significant changes in the aircraft configuration. One of the problems that these configurations try to overcome is related to the occurrence of the dynamic stall on the retreating blade that limits the high speed performance of classical helicopter rotor configurations [1]. Indeed, it is possible to mitigate or suppress the effect of dynamic stall by using several passive or active control techniques on a conventional rotor configuration. Many recent activities analysed the effectiveness of different control systems integrated into the blade section in order to improve helicopter performance and expand the flight envelope and vehicle utility. Currently, improvements to control rotor blade dynamic stall rely upon the optimization of the blade airfoil shape by introducing, for example, a variable droop leading edge [5]. Moreover, the use of blowing devices such as air-jet vortex generators [6] or plasma actuators [7] represents an attractive solution for the reduction of the airloads hysteresis and the suppression of stall-driven flutter occurring during a blade pitching cycle [3]. Moreover, the research on dynamic stall is now focusing on the evaluation of reliable modeling for the simulation of this highly unsteady phenomenon characterised by the rapid formation, migration and shedding of strong vortices, as in the case of deep dynamic stall regime [8, 9]. The validation of such numerical models requires thorough comparison between the simulations results and a comprehensive experimental data base, in particular for the deep dynamic stall conditions.

A new experimental-numerical activity started at Politecnico di Milano on this topic. The focus of this work is the evaluation of different CFD models with respect to the experimental results. Wind tunnel tests were carried out on a pitching NACA 23012 blade section. The airfoil was selected since, being a typical helicopter blade airfoil, it was employed in experimental activities in the past years about the study of the dynamic stall phenomenon on pitching blade sections [11, 12]. The experimental rig was designed to reproduce the deep dynamic stall condition for a full-scale helicopter rotor blade section. Moreover, the experimental set up is suitable for different measurement techniques as unsteady pressure measurements, obtained from miniature pressure transducers installed on the midspan airfoil contour and Particle Image Velocimetry, which makes it possible to completely characterise the time-dependent flow field and consequently achieve a detailed insight of the different stages of the dynamic stall process.

The main goal is to obtain reliable models that could be used in the phase of development and sizing of new control devices for dynamic stall effect mitigation. The experimental campaign carried out on the pitching blade section highlighted the occurrence of three dimensional effects on the flow phenomena. Consequently, an other interesting focus of the work is to evaluate the importance of such three dimensional effects introduced by the intrinsic nature of the dynamic stall phenomenon as well as by the use of a finite span model and by the wind tunnel side walls. For this purpose, both two and three-dimensional models were built using EDGE [13], a compressible Navier-Stokes solver developed at FOI, the Swedish Research Agency. In the paper, the experimental results for deep dynamic stall conditions are presented together with a thorough comparison with the different numerical results.

2 Experimental set up

The experimental activity was conducted at Politecnico di Milano in the low-speed closed-return wind tunnel of the Aerodynamics Laboratory of the Aerospace Department. The wind tunnel has a rectangular test section with 1.5 m height and 1 m width. The maximum wind velocity is 55 m/s and the freestream turbulence level is less than 0.1%.

The aluminium machined airfoil model, with chord $c = 0.3$ m and span $b = 0.93$ m, has an interchangeable midspan section for the different measurements techniques employed, one for PIV flow surveys (see Fig. 1) and another for unsteady pressure measurement equipped with pressure taps positioned along the midspan chord line. The model is pivoted around two external steel shafts corresponding to the 25% of the airfoil chord. The model pitching motion is provided by a brushless servomotor with a 12:1 gear drive (see Fig. 2).

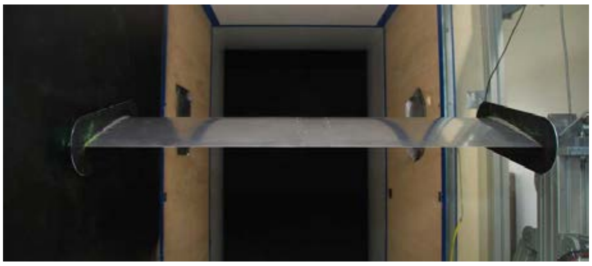

Figure 1: NACA 23012 blade section model inside the wind tunnel tests section in PIV mode.

The time history of the lift and pitching moment during a pitching cycle was evaluated by integration of the phase averaged pressures collected over 30 complete pitching cycles. The phase average of the pressure signals was computed using a bin of 0.1° angle of attack amplitude. The pressures were measured by means of 21 Kulite fast-response pressure transducers located inside the model interchangeable midspan section.
The PIV system used a double shutter CCD camera with a 12 bit, 1280 × 1024 pixel array and a Nd:Yag double pulsed laser, with 200 mJ output energy and wavelength 532 nm. In order to get a better resolution of the image pairs, the measurement area covering the whole airfoil upper surface was composed by four $103mm \times 82$ mm measurement windows spanning the chord direction.
A more detailed description of the pitching airfoil experimental rig and of the measurement techniques set up can be found in Zanotti et al. [10].

3 CFD model

The CFD solver used for this study is the EDGE code developed by FOI, the Swedish Defence Research Agency [13]. The code is capable of solving flows with different regimes from inviscid to fully turbulent using various turbulence models. RANS (Reynolds-Averaged Navier-Stokes), DES (Detached-Eddy Simulation) and LES (Large Eddy simulation) models in 2/3 dimensions are considered in this code. In the present work, URANS simulations were carried out using the Hellsten $k-\omega$ turbulence model recalibrated fully consistently with the EARSM (Explicit Algebraic Reynolds Stress Model) assumption by Wallin & Johansson to define the relation between Reynolds stresses and strain rate tensor [14, 15]. The flow equations in an Arbitrary Lagrangian Eulerian (ALE) framework read

$$\frac{d}{dt}\int_v \mathbf{u} dv = -\int_s \left[F_I(\mathbf{u}) + F_V(\mathbf{u}) - \mathbf{u}\dot{\mathbf{x}}_\mathbf{f}\right] ds \quad (1)$$

where $\mathbf{u} = [\rho, m, E^t]$ is the vector of the conservative variables density, momentum and total energy per unit volume, and $F_I(\mathbf{u})$ and $F_V(\mathbf{u})$ are the inviscid and viscous flux matrices, respectively. In the above equations, v_i is the control volume, s is its surface and $\dot{\mathbf{x}}_f(\mathbf{s}, t)$ is the local velocity of the surface.

3.1 Grid generation

For the computation on a 2D model, a C-grid topology was used with a structured grid made of 1100×190 ($N_x \times N_y$) quadrilateral elements, see Fig. 3. The wall normal grid resolution of the closest internal node from wall is of the order of $y^+ = 1$, as the distance of this node is chosen about about 10^{-5} c. The location of the farfield is set to be at 20 c length away from the airfoil wall. The baseline of the 3-D computational mesh is made of 560 × 130 quadrilateral elements, see Fig. 4. This sectional 2D grid was extended 1.5 c lenght in the spanwise direction ($\frac{b}{c} = 1.5$) with a uniform Δz spacing around 0.025 ($N_z = 60$) to construct the 3D mesh. The computational domain was decomposed into 36 subdomains that were distributed among processors using MPI technique.
A no-slip adiabatic condition and slip wall condition were employed respectively along the airfoil surface and on both side boundaries. A characteristic boundary condition was also prescribed along far-field boundary. In all computations, a sinusoidal pitching motion is imposed on the whole grid which is treated like a rigid body.For the 2D computations 200 physical time steps per period were considered while

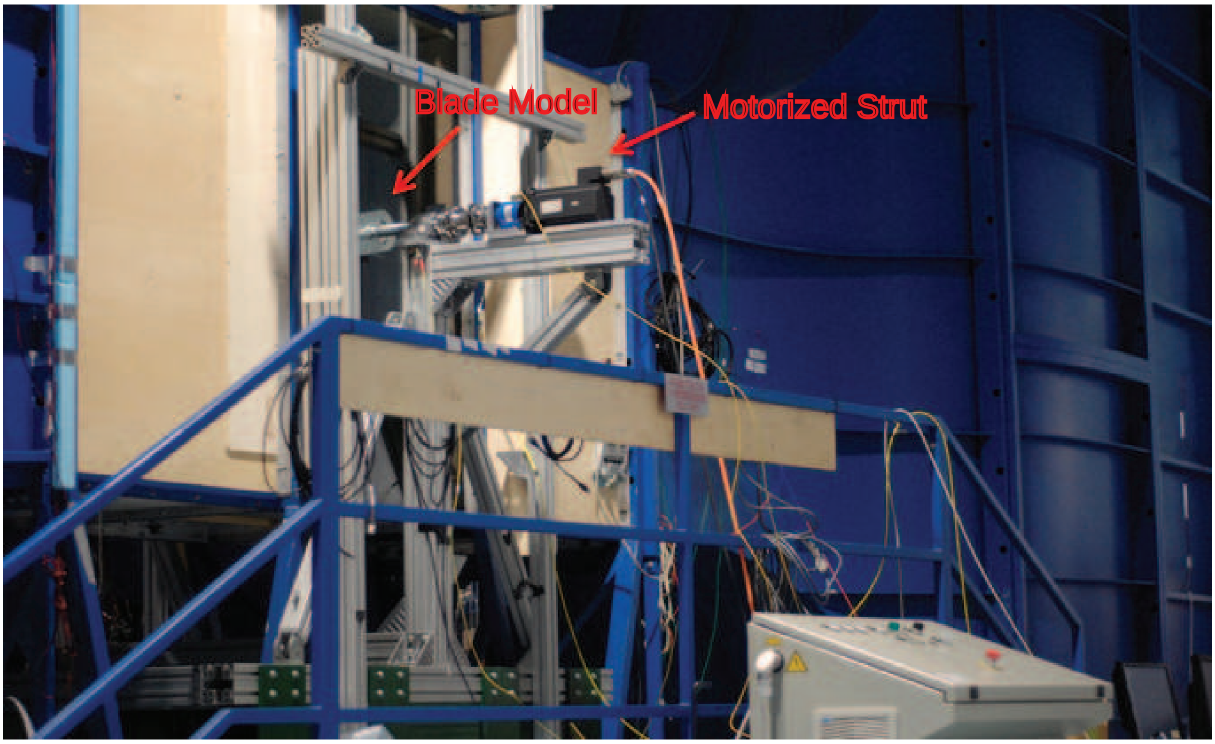

Figure 2: Experimental rig for pitching airfoils.

for the 3D computations 68 physical time steps per period were considered. The numerical results were extracted after 4 cycles to ensure a periodic state.

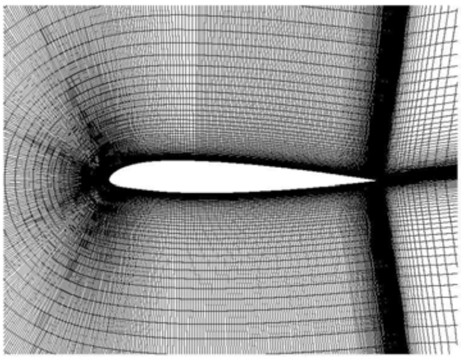

Figure 3: NACA 23012 2D grid.

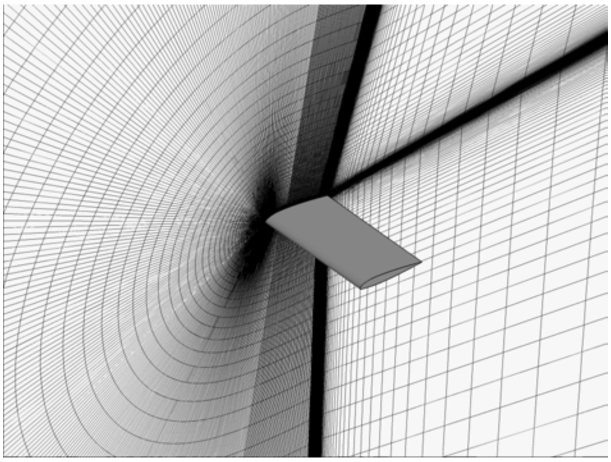

Figure 4: NACA 23012 3D grid.

4 Results

The dynamic stall conditions considered for modeling assessment are pitching cycles characterised by a mean angle of attack $\alpha_m = 10°$ and 15° with a constant oscillation amplitude $\alpha_a = 10°$ and reduced frequency $k = 0.1$. These conditions correspond to the deep dynamic stall regime [1]. The pitching condition was tested at relatively low speed (30 m/s), corresponding to $Re = 6 \cdot 10^5$ ($Ma = 0.09$), respect to the test rig capability, because the long run time required by the present PIV measurement would produce, at a higher velocity, a too long highly stressing load cycle on the model strut. Figure 5 presents the comparison between the measured lift and quarter chord moment coefficients against the results of the 2D and 3D simulations. The standard deviation of the airloads coefficients are plotted on the experimental airloads curves.

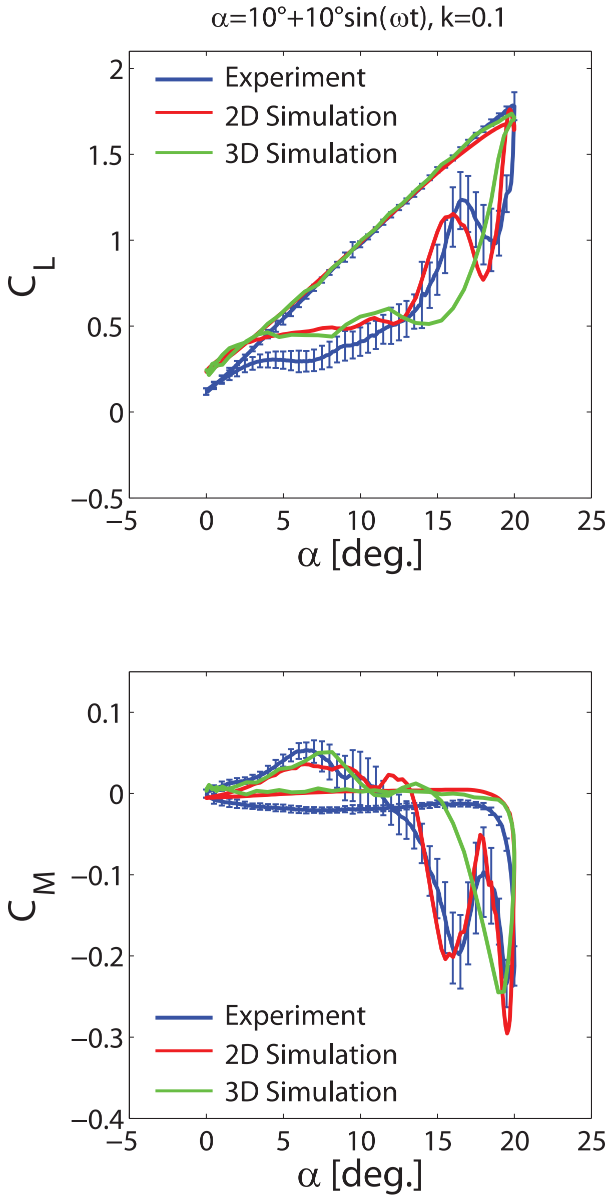

Figure 5: Comparison of experimental and numerical airloads for $\alpha = 10° + 10° sin(\omega t)$, $k = 0.1$ ($Re = 6 \cdot 10^5$).

For the test case with $\alpha_m = 10°$, the airloads comparison shows some discrepancies between the 2D and 3D models results with the wind tunnel data. During the upstroke motion, where the flow on the airfoil upper surface is fully attached, the lift coefficient curve slope evaluated by 2D simulations is a lower than the experimental one while the slope of the 3D simulation curve seems to be fairly in good agreement with the experimental one. During the downstroke motion the flow field is characterised by the formation of strong vortices moving on the airfoil upper surface that produce large oscillations of the airloads. The 2D numerical model reproduce very well the hysteresis and the oscillations of the lift and pitching moment curves observed in the experimental data. In particular, the airloads oscillations in downstroke presents a delay in angle of attack for the numerical models in respect with the experimental curves, higher for the 3D model. This behavior could be explained by the use of a finer mesh for the 2D model that allowed to capture more accurately the variation of pressure distribution on the airfoil surface produced by the rapid migration of the vortices on the airfoil upper. Moreover, the experimental peak of the pitching moment coefficient occurring at the top of the upstroke motion is very well captured by the 3D numerical model.
The quite correct numerical evaluation of both pitching moment peak and its aerodynamic damping in deep dynamic stall regime could be considered a very interesting result as represents the main goal to be assessed during the development and sizing phase of new control devices for the mitigation of dynamic stall phenomenon.

For the case with $\alpha_m = 15°$, the numerical lift curves for both the 2D and 3D simulations present a delay of the non-linear increase in slope due to the formation and migration of the DSV in respect to the experimental curve, as can be observed in Fig. 6. Moreover, the 2D simulation results present a peak of lift and pitching moment greater than the measured ones. The higher values of lift and pitching moment coefficients could be explained by an overestimation of the vortices magnitude in the 2D numerical simulations. In fact, the 3D simulation results present a peak of the lift coefficient similar to the experimental value. During the downstroke motion, the hump observed in the airloads curves evaluated by both the 2D and 3D numerical models is delayed respect to the experimental one.

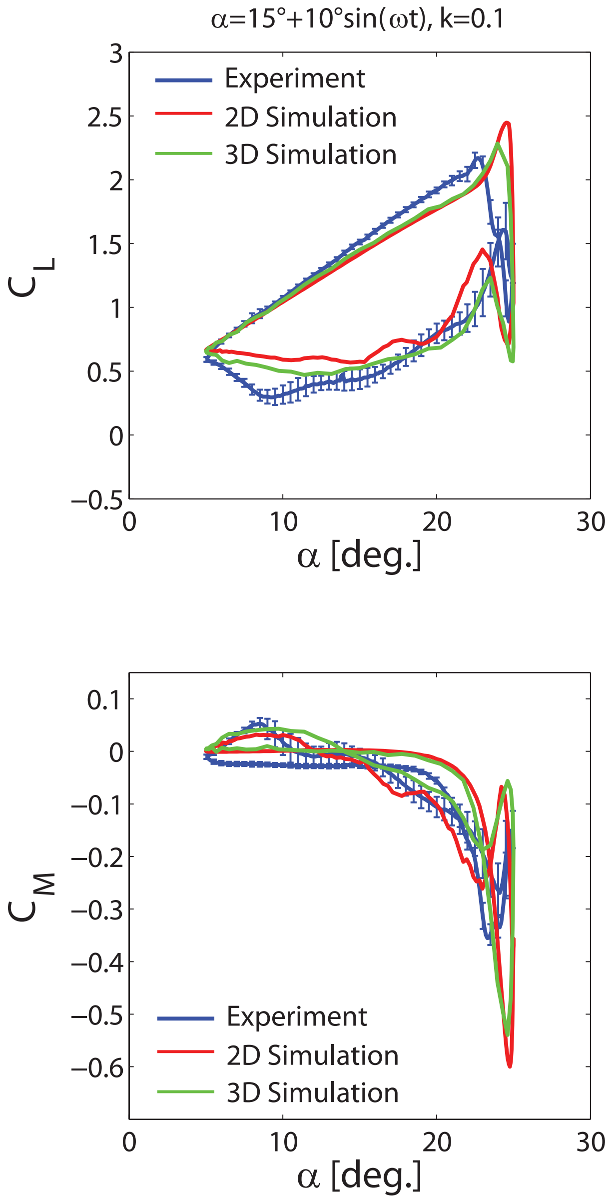

Figure 6: Comparison of experimental and numerical airloads for $\alpha = 15° + 10° sin(\omega t)$, $k = 0.1$ ($Re = 6 \cdot 10^5$).

The PIV results at model midspan were compared to the velocity fields obtained by the 2D and 3D simulations to assess the modeling capabilities of the numerical models to reproduce the flow physics involved in the phenomenon, focusing the attention on the differences produced on the aerodynamic phenomena by three-dimensional effects. In the following Figures the velocity fields are shown by means of instantaneous streamlines patterns; the illustrated 3D numerical flow field is evaluated at midspan.

Figures 7 and 8 show the comparison between the experimental and numerical flow field at four angles of attack of interest for the test case with $\alpha_m = 10°$.

At $\alpha = 18°$ in upstroke, corresponding to a post-stall condition in steady case, the flow field on the airfoil upper surface is fully attached, as shown in Fig. 7(a): the flow separation is delayed by a reduction in adverse pressure gradients produced by a kinematic induced camber effect due to the positive rapid pitching rate [2]. For this condition both the 2D and 3D numerical model reproduce well the experimental flow field at midspan.

For the present test case, the flow separation does not occur during almost the complete upstroke motion. In fact, the flow separation starts only at the end of the upstroke motion, as illustrated in the flow field at $\alpha = 20°$ in Fig. 7(b). The PIV flow field, for this angle of attack shows a flow separation spread over more than half of the airfoil chord characterised by small vortex structures within the separated flow region. The numerical flow fields present a single extended vortex structure at the trailing edge; in particular, the 3D model captures the extension of the separation region on the airfoil upper surface better than the 2D model (see Figures 7 (d) and (f)).

During the downstroke motion the flow on the airfoil upper surface is fully separated and it is characterised by the formation, migration and shedding of strong vortices. In fact, at $\alpha = 18°$ in downstroke the measured flow field presents a small vortex near the leading edge and a very large vortex at about half of the chord, as illustrated in Fig. 8(a). The aerodynamic features shown by the 3D numerical flow field are in quite good agreement with the experimental flow survey (see Figure 8(c)), while the 2D numerical flow field shows two counter-rotating vortices near the trailing edge region (see Figure 8(e)).

Also at $\alpha = 16°$ in downstroke the experimental and the 3D numerical flow fields present a good agreement. In fact, the simulation reproduces the extended region of reversed flow on the upper surface, a small vortex near the leading edge and a larger size vortex

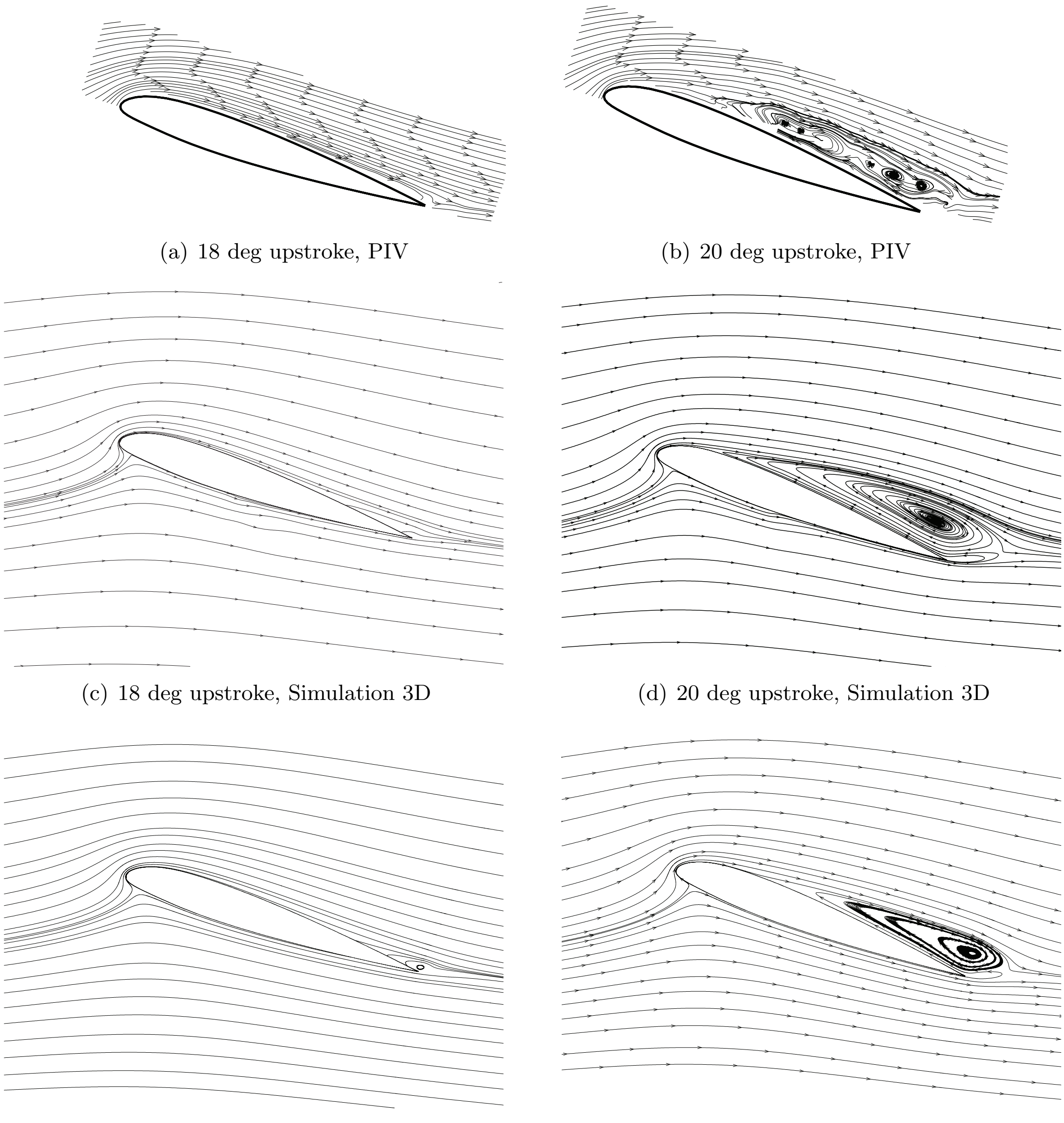

(a) 18 deg upstroke, PIV

(b) 20 deg upstroke, PIV

(c) 18 deg upstroke, Simulation 3D

(d) 20 deg upstroke, Simulation 3D

(e) 18 deg upstroke, Simulation 2D

(f) 20 deg upstroke, Simulation 2D

Figure 7: Comparison of experimental and numerical flow fields for $\alpha = 10^{\circ} + 10^{\circ} sin(\omega t)$, $k = 0.1$.

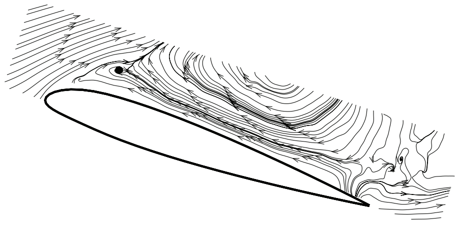

(a) 18 deg downstroke, PIV

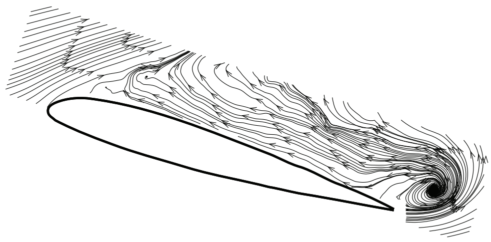

(b) 16 deg downstroke, PIV

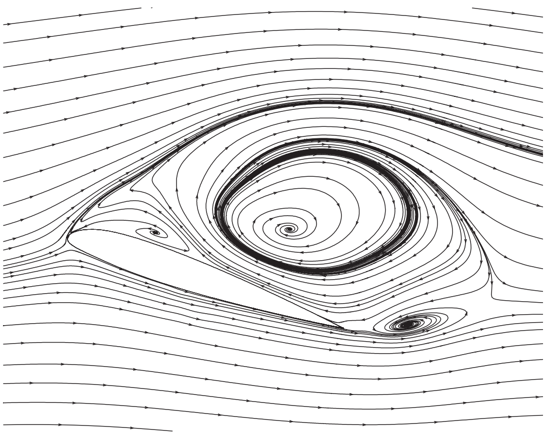

(c) 18 deg downstroke, Simulation 3D

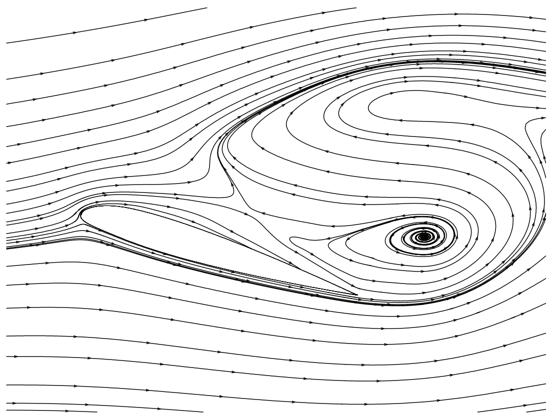

(d) 16 deg downstroke, Simulation 3D

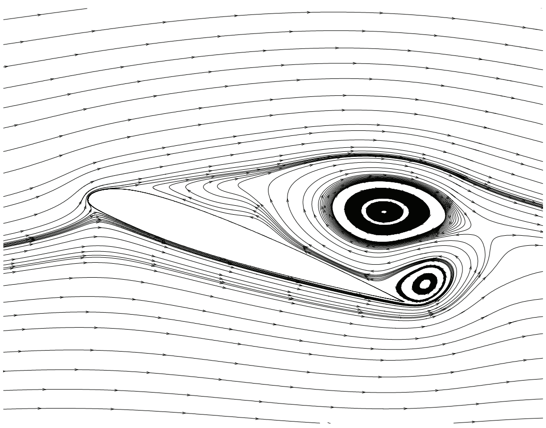

(e) 18 deg downstroke, Simulation 2D

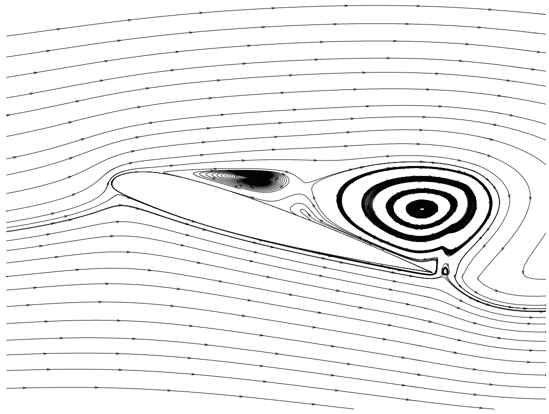

(f) 16 deg downstroke, Simulation 2D

Figure 8: Comparison of experimental and numerical flow fields for $\alpha = 10^{\circ} + 10^{\circ} sin(\omega t)$, $k = 0.1$ (Continued).

detaching the trailing edge, as shown in Fig. 8(b). The large recirculating flow region on the upper surface recalls air from the airfoil lower surface causing the formation of this counter-clockwise vortex located very close to the trailing edge (see Figure 8(d)). The 2D simulation, again, does not succeed to capture the experimental flow field in this condition (see Figure 8(f)).

Figures 9 and 10 show the comparison between the experimental and numerical flow field at four angles of attack of interest for the test case with $\alpha_m = 15°$.
At $\alpha = 23°$ the flow field on the airfoil upper surface shows the DSV structure. In particular, at this angle of attack the DSV reaches the airfoil midchord and extends over about the 50% of the airfoil upper surface, as it can be observed in Fig. 9(a). The 3D simulation captures very well the flow physics concerning the DSV occurrence (see Fig. 9(c)). The 2D simulation flow field shows, as can be observed in Fig. 9(e) the onset of flow separation at the trailing edge region that represents a preliminary stage before DSV formation; consequently, for the 2D simulation the DSV formation presents a delay in respect to the 3D simulation and to the experiment.
Increasing the angle of attack, the DSV grows and moves downstream as shown in Fig. 9(b) for $\alpha = 24°$. The growth of DSV is again well captured by the 3D simulation (see Fig. 9(d)), while the 2D simulation shows, for this angle of attack, a flow field similar to the 3D simulation and to the experimental ones, but obtained at $\alpha = 23°$; this feature confirms the delay of the flow physics captured by the 2D model.
At the maximum incidence of the oscillating cycle, $\alpha = 25°$, where the airfoil reverses the pitching motion, the PIV flow field shows that DSV has definitively left the airfoil and a small counter-clockwise vortical structure can be observed at the trailing edge (see Fig. 10(a)). The flow on the airfoil upper surface is fully separated and the reversed flow region is extended over the entire airfoil chord within the measurement window area. The behavior of the flow physics captured by the 2D and 3D numerical models presents some differences with respect to the experimental flow field (see Fig. 10(c) and (e). In fact, both the simulations results show, for this angle of attack, an extended clockwise vortex very close to the airfoil upper surface, while at the trailing edge region the numerical flow fields present a counter-clockwise vortex in agreement to the PIV measurements.
During the downstroke motion the flow field on the airfoil upper surface is fully separated and characterised by the migration of vortical structures on the airfoil upper surface, as can be observed at $\alpha = 18°$ in Fig. 10(b). For this angle of attack the two vortices shown by PIV measurements are well captured by the numerical models (see Fig. 10(d) and (f)).
The good agreement between the experimental flow field with the 3D simulation results demonstrates that strong three-dimensional effects characterise the performance of the airfoil tested in the wind tunnel under deep dynamic stall conditions. These 3D flow features could be produced in part by the intrinsic three-dimensional nature of dynamic stall phenomenon but also they could be related to the three-dimensional effects induced by the use of a finite-span model and by the wind tunnel side walls. The analysis of the 3D simulations results enabled to point out the phase of the pitching cycle where these 3D effects are consistent. Figure 11 shows the 3D simulations results for the test case with $\alpha_m = 10°$ illustrated by the 3D streamlines patterns around the model surface together with the pressure coefficient distribution on the model surface, for the four angles of attack considered in the flow field comparison.
At $\alpha = 18°$ and $\alpha = 20°$ in upstroke the spanwise pressure distribution is quite uniform along the whole model span and strong three-dimensional effects are not appreciable (see Fig. 11(a) and (b)).
At $\alpha = 18°$ and $\alpha = 16°$ during downstroke, 3D vortex structure shed downstream produces a strong alteration of pressure distribution on the whole model surface up to the tip (see Fig. 11(c) and (d)).
The strong modification of the spanwise pressure and velocity field justifies the differences observed during downstroke motion between the 2D simulation and the experimental results

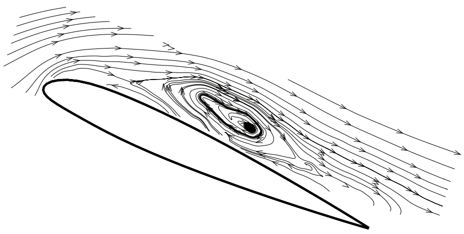

(a) 23 deg upstroke, PIV

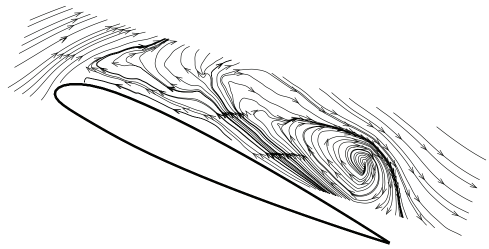

(b) 24 deg upstroke, PIV

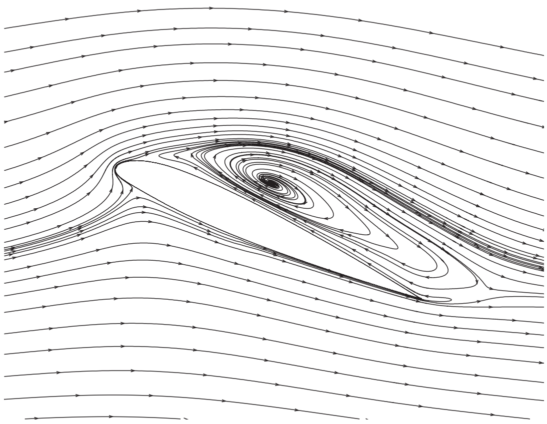

(c) 23 deg upstroke, Simulation 3D

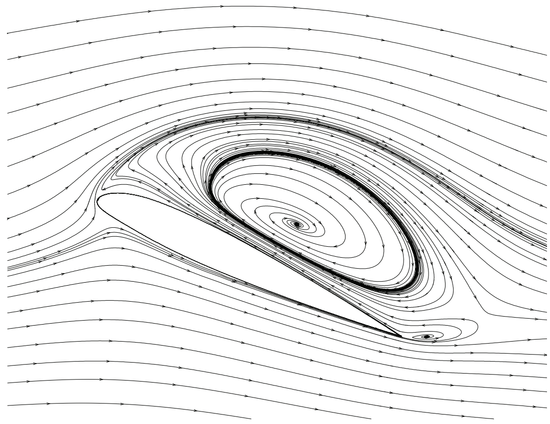

(d) 24 deg upstroke, Simulation 3D

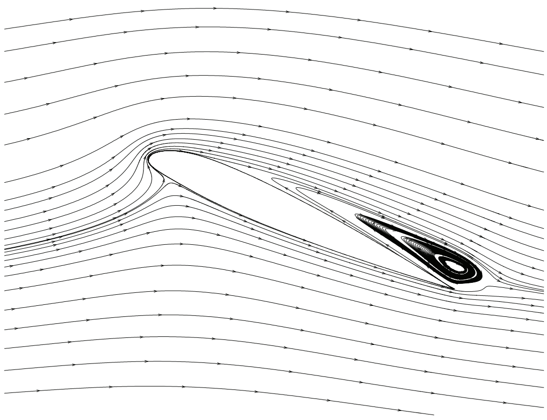

(e) 23 deg upstroke, Simulation 2D

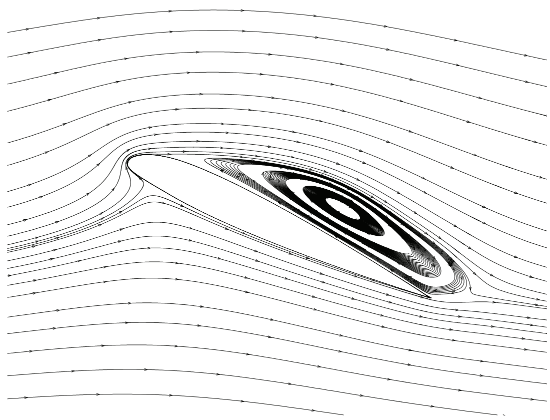

(f) 24 deg upstroke, Simulation 2D

Figure 9: Comparison of experimental and numerical flow fields for $\alpha = 15^\circ + 10^\circ sin(\omega t)$, $k = 0.1$.

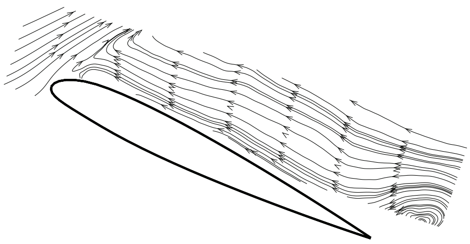

(a) 25 deg upstroke, PIV

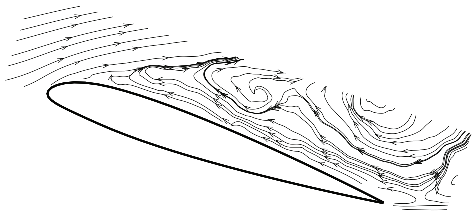

(b) 18 deg downstroke, PIV

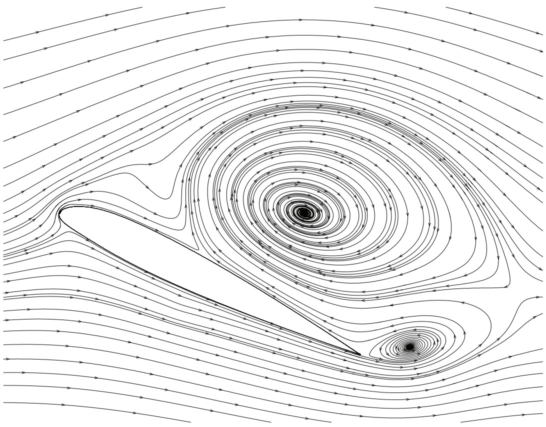

(c) 25 deg upstroke, Simulation 3D

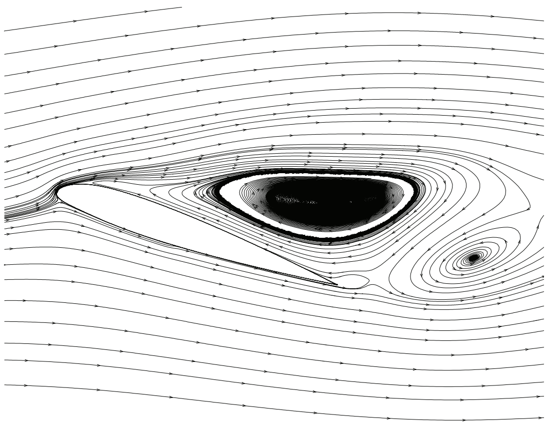

(d) 18 deg downstroke, Simulation 3D

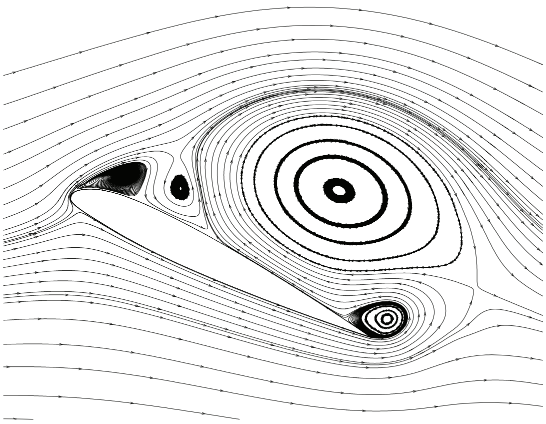

(e) 25 deg upstroke, Simulation 2D

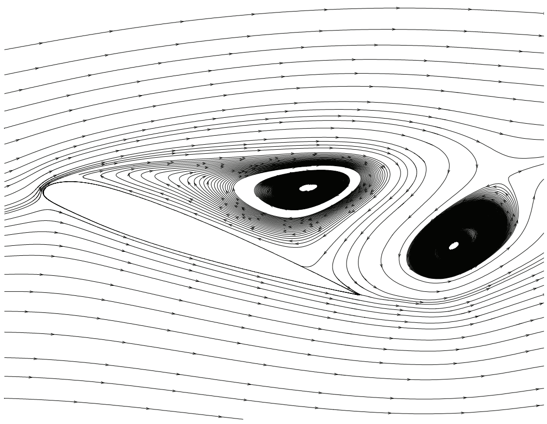

(f) 18 deg downstroke, Simulation 2D

Figure 10: Comparison of experimental and numerical flow fields for $\alpha = 15^{\circ} + 10^{\circ} sin(\omega t)$, $k = 0.1$ (Continued).

about the flow physics involved in the dynamic stall phenomenon.

5 Conclusions

CFD models for the NACA 23012 pitching airfoil were developed in order to compare results against wind tunnel data and to assess the capabilities of CFD tools when facing with such a demanding aerodynamic phenomenon. The comparison of numerical and experimental results made possible to clarify the importance of three-dimensional effects on the flow phenomena involved in the deep dynamic stall regimes. For deep dynamic stall conditions the 2D model demonstrates the capability to reproduce the measured airloads hysteresis and oscillations during downstroke motion, due to the use of a very fine mesh. The 2D model fails to reproduce the detailed flow physics involved in the phenomenon evaluated by the PIV surveys at the model midspan.
The comparison of the 3D simulations results with the experimental data demonstrated that three-dimensional effects influences the flow field over the pitching airfoil during wind tunnel tests in deep dynamic stall regime. These three-dimensional effects on the flow phenomena are particularly consistent in post-stall conditions and could be due to the intrinsic three-dimensional nature of dynamic stall, to the usage of a finite-span wind tunnel model and to the wind tunnel walls. In fact, the flow field obtained by the 3D simulations captures well the fine details of the dynamic stall phenomenon observed by the PIV surveys and in particular the formation and shedding of strong vortex structures that move quickly on the airfoil upper surface.
The good reliability of the numerical models built using the EDGE code for dynamic stall performance assessments and the analysis of the three-dimensional effects occurring during experiments on pitching airfoils represent the main goals of this activity. In particular, the capability demonstrated by the numerical simulations to evaluate the airfoil performance and the flow physics involved in the deep dynamic stall regime is an important tool for the study of new airfoils to be employed on helicopter blades and for the sizing of new control devices for dynamic stall effect mitigation.

References

[1] W.J. McCroskey. The Phenomenon of Dynamic Stall, NASA TM 81264, 1981.

[2] J.G. Leishman. Principles of helicopter aerodynamics, Cambridge Aerospace Series, 2000.

[3] F.O. Carta. An Analysis of the Stall Flutter instability of Helicopter Rotor Blades, *Journal of American Helicopter Society*,**12**, 1-8, 1967.

[4] L.K. Loftin Jr. and H.A. Smith. Aerodynamic characteristics of 15 naca airfoil sections at seven Reynolds numbers, NACA Technical Report, Langley Aeronautical Laboratory, 1949.

[5] M. Chandrasekhara, P. Martin and C. Tung. Compressible Dynamic Stall Control Using a Variable Droop Leading Edge Airfoil, *Journal of Aircraft*, **41**, 862-869, 2004.

[6] C. Singh, D. Peake, A. Kokkalis, V. Khodagolian, F. Coton and R. Galbraith. Control of Rotorcraft Retreating Blade Stall Using Air-Jet Vortex Generators, *Journal of Aircraft*, **43**, 1169-1176, 2006.

[7] M. Post and T. Corke. Separation Control Using Plasma Actuators: Dynamic Stall Vortex Control on Oscillating Airfoil, *AIAA Journal*, **44**, 3125-3135, 2006.

[8] M.R. Visbal. Numerical Investigation of Deep Dynamic Stall of a Plunging Airfoil, *AIAA Journal*, **49**, 2152-2170, 2011.

[9] M. Costes, F. Richez, A. Le Pape and R. Gavériaux. Numerical investigation of three dimensional effects during dynamic stall, 37th European Rotorcraft Forum, 13-15 September, Gallarate (VA), Italy, 2011.

[10] A. Zanotti, F. Auteri, G. Campanardi and G. Gibertini. An Experimental Set Up for

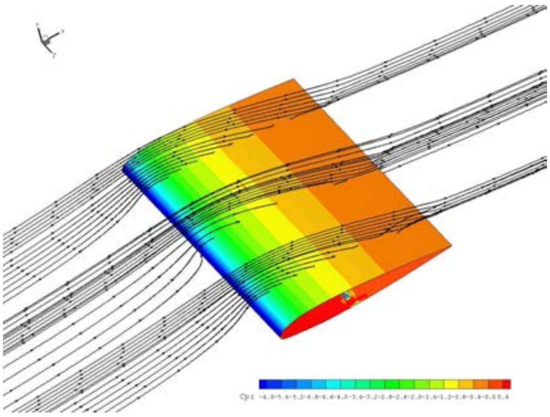

(a) 18 deg upstroke

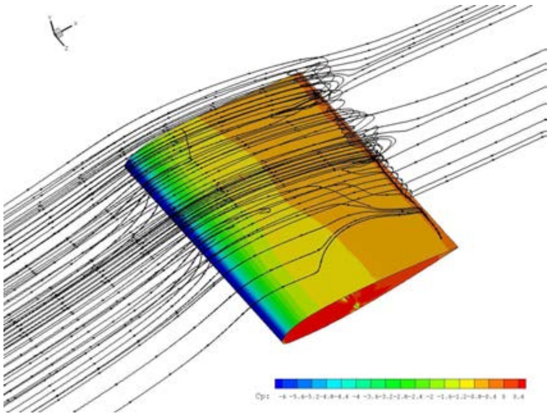

(b) 20 deg upstroke

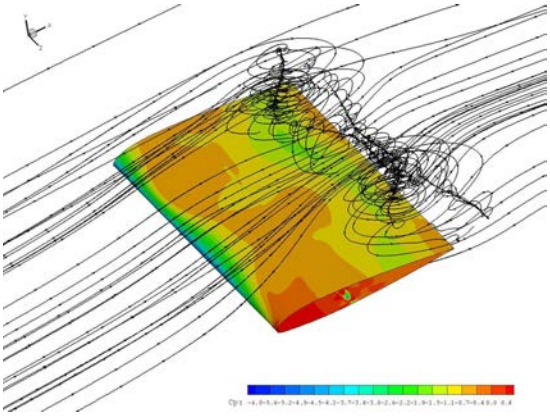

(c) 18 deg downstroke

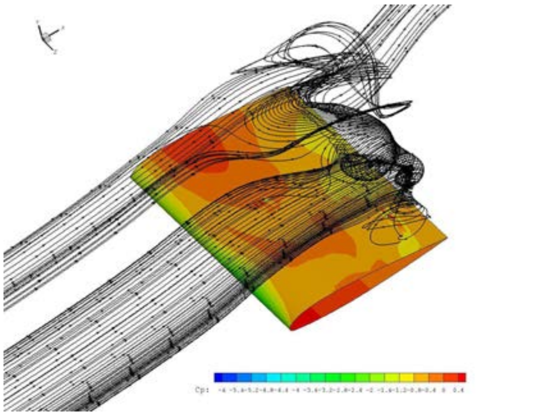

(d) 16 deg downstroke

Figure 11: 3D simulation results for $\alpha = 10^{\circ} + 10^{\circ} sin(\omega t)$, $k = 0.1$: 3D streamline patterns and pressure coefficient distribution on the model surface.

the Study of the Retreating Blade Dynamic Stall, 37th European Rotorcraft Forum, 13-15 September, Gallarate (VA), Italy, 2011.

[11] J.G. Leishman. Dynamic stall experiments on the NACA 23012 aerofoil, *Experiments in Fluids*, **9**, 49-58, 1990.

[12] M. Raffel, J. Kompenhans, B. Stasicki, B. Bretthauer and G.E.A. Meier. Velocity measurement of compressible air flows utilizing a high-speed video camera, *Experiments in Fluids*, **18**, 204-206, 1995.

[13] P. Eliasson. EDGE, a Navier-Stokes solver for unstructured grids. *Proc. to Finite Volumes for Complex Applications III*, Vol.1, pp.527-534, 2002.

[14] S. Wallin. Engineering turbulence modeling for CFD with a focus on explicit algebraic Reynolds stress models, *Doctoral Thesis Norsteds Tryckeri AB*, Stockholm, Sweden,2003.

[15] A. Hellsten. New advanced $k - \omega$ turbulence model for high-lift aerodynamics, *AIAA Journal*, Vol. 43, No.9, pp.1857-1869, 2005.